Catalysis Today 420 (2023) 114083

Contents lists available at ScienceDirect

Catalysis Today

journal homepage: www.elsevier.com/locate/cattod

Bifunctional oxygen electrocatalysts based on non-critical raw materials: Carbon nanostructures and iron-doped manganese oxide nanowires

N.I. Villanueva-Martínez [a], C. Alegre [a,*], I. Martínez-Visús [b,c], M.J. Lázaro [a,*]

[a] Instituto de Carboquímica, CSIC, C/. Miguel Luesma Castán, 4, 50018 Zaragoza, Spain
[b] Instituto de Nanociencia y Materiales de Aragón (INMA), CSIC - Universidad de Zaragoza, Zaragoza 50018, Spain
[c] Chemical and Environmental Engineering Department, Universidad de Zaragoza, Zaragoza 50018, Spain

ARTICLE INFO

Keywords:
Bifunctional catalysts
Carbon nanofibers
Manganese oxide
Oxygen reduction
Oxygen evolution

ABSTRACT

Alkaline metal-air batteries are unique systems for energy storage. These devices require a bifunctional catalyst in the positive electrode that must perform both the oxygen evolution and reduction reactions (OER and ORR, respectively). Generally, cobalt-based oxides are employed as air electrodes; however, cobalt is a critical raw material. Future battery devices will mandatorily need non-critical raw materials based on highly abundant metals. Here we investigate the feasibility of iron-doped manganese oxide in the form of nanowires (Fe-MONW) combined with carbon nanofibers. MnO_2 is known for being active for the ORR, however its activity towards the OER is not yet fully understood. Carbon nanofibers (CNF) on the other hand, provide the necessary electrical conductivity to the catalytic system. Simple methods and economic materials are employed to synthesize the Fe-MONW/CNF composites. Our results show that there is a synergistic effect between CNF and MONW, especially for the ORR, which manifests in an increase in the number of exchanged electrons– from 2.9 to 3.5 – and a shift in the onset potential of 70 mV. Doping MONW with iron further enhances the catalytic activity, for both the ORR and OER. Fe ions generate defects in the manganese oxide structure, favoring the adsorption of oxygen and eventually enhancing the catalytic activity. Fe-doped-MONW shows onset potentials for OER comparable to the benchmark catalyst, IrO_2. The improvement on the catalytic activity is particularly evident in terms of the reversibility gap, ΔE. ΔE is the difference between the potential when the current density is 10 mA cm^{-2} in OER and the half-wave potential for the ORR, being a fundamental parameter to assess the performance of metal-air batteries. The reversibility gap for the best catalyst, 5Fe-MONW/CNF, is $\Delta E = 922$ mV (140 mV lower than non-doped MONW/CNF and between 160 and 320 mV lower than the individual components, MONW and CNF). Endurance tests show remarkable stability of the iron-doped MONW/CNF, with a stable potential and an even lower ΔE of 800 mV for *ca.* 20 h of operation (charge-discharge cycles at ± 10 mA cm^{-2}).

1. Introduction

The interest of the scientific community in metal-air batteries (MABs) is continuously increasing since MABs are considered promising energy storage devices. MABs present high theoretical energy densities (from 1000 Wh kg^{-1} of Fe-air batteries to 11.000 Wh kg^{-1} of Li-O_2 batteries) [1,2]. A wide variety of abundant metals can be used as anodes, *e.g.*, Fe, Zn, Mg, Al, or Si, which is of high interest since the supply chain of batteries' raw materials is a significant concern [3–5]. An additional advantage of metal-air batteries is that certain metal anodes, like Fe or Zn, operate in aqueous alkaline media, with lower toxicity (compared to organic electrolytes) and favoring the use of low-cost non-noble metals for the air electrode [5,6]. The air electrode of aqueous metal-air batteries is responsible for reducing oxygen (during the discharge of the battery) and oxidizing water (during the charge), carrying out the widely known couple "oxygen reduction and oxygen evolution reactions (ORR/OER)" [7,8]. It is generally acknowledged that oxygen electrocatalysis is a major challenge for researchers, given the sluggish kinetics and multiple steps of these reactions. Besides, the OER entails a further challenge, the high operating potential (> 1.5 V vs. RHE), producing the electrochemical corrosion of the electrode components [9,10]. These features force research into the quest for highly active, durable, and bifunctional catalysts.

From noble metals to transition metals, several catalysts have been

* Corresponding authors.
E-mail addresses: cinthia@icb.csic.es (C. Alegre), mlazaro@icb.csic.es (M.J. Lázaro).

https://doi.org/10.1016/j.cattod.2023.114083
Received 30 November 2022; Received in revised form 24 February 2023; Accepted 5 March 2023
Available online 9 March 2023

investigated in the last years for metal-air batteries [11–16]. Among non-noble metals, cobalt-based oxides with structures such as spinels or perovskites are widely known for their bifunctionality for ORR/OER [8,17–22]. However, due to its use in lithium-ion cathodes, cobalt is a critical raw material, with increasing demand and availability concerns. Low-cost alternative metals with high activity are then sought to avoid the use of cobalt in these devices.

Manganese oxides have been investigated as an alternative to cobalt-based catalysts, due to their promising activities, particularly for the ORR, and more recently, with good performances for the OER [23–25]. Yin et al., in a recent review, summarized the main advantages of MnO_2-based catalysts such as the diversity of nanostructures that they can present (tubes, sheets, rods, wires) and different crystallinity (α-, β-, γ-, σ- and λ-MnO_2) what confers them a high surface-area utilization and a rich redox chemistry [26,27]. All these features provide them with an interesting compromise of activity and stability [28]. Gu et al. investigated several manganese nanostructures, determining that manganese nanowires have the best features as ORR/OER catalysts, however, at the expense of using ionic liquids [29]. Some authors have proved that doping MnO_2 with Ni, Fe, or Co is beneficial for their activity towards ORR and OER [28]. However, the low conductivity of these oxides is often an issue for further application. For this reason, the mixture of manganese-based oxides with conductive carbon materials has been recently investigated [30]. Previous reports in the literature have shown good performances combining MnO_2 with graphene, carbon nanotubes, or carbon nanospheres [4,31–33]. For example, Levy et al. employed CNT to improve the activity of MnO_2-catalysts for Li-O_2 batteries. Miao et al. combined MnO_2 with nitrogen-doped graphene as a flexible air electrode for solid-state zinc-air batteries [34].

Here we propose the use of highly-graphitic CNFs as a conductive additive for enhanced ORR/OER bifunctional catalysts based on low-cost iron doped-manganese oxide nanowires. Low-cost catalysts based on non-critical-raw materials are essential for developing economic and sustainable energy storage electrochemical devices such as metal-air batteries or regenerative fuel cells, requiring both bifunctionality and durability.

2. Experimental

2.1. Materials and methods

All the chemicals employed were purchased as high-purity reagents and used as received. The synthesis of manganese oxide nanowires consisted in an easily scalable, low-cost hydrothermal process previously established by Xiao et al. [35]. Briefly, 0.63 g of $KMnO_4$ (99%, Panreac) and 1.4 mL of HCl (37%, Fluka) were mixed and magnetically stirred for 30 min in 50 mL of deionized water. Afterward, the former solution was transferred to a Teflon-lined stainless steel autoclave, placed in an oven for 12 h at 120°C or 140°C. Once the autoclave cooled down, the brown precipitate obtained was collected and washed with deionized water in a centrifuge until the waste water had a neutral pH. The obtained powder was dried overnight at 65°C to obtain the manganese oxide nanowires, named MONW-X, where X is the temperature of the autoclave, either 120°C or 140°C. The same procedure was employed to obtain iron-doped manganese oxide nanowires by adding different amounts (28, 56, or 84 mg) of $FeCl_3$ (97%, Sigma-Aldrich) in the precursor solution, aiming to obtain nominal loadings of 2, 5, and 7 wt%. Fe-doped MONW will be named as X-Fe-MONW, where X is the actual Fe loading determined by ICP.

Once obtained, MONW and Fe-doped MONW were mechanically mixed with highly-graphitic carbon nanofibers obtained by catalytic decomposition of methane, as described in previous reports [36]. Briefly, 300 mg of a Ni:Cu:Al_2O_3 (78:8:16 at. ratio) catalyst were introduced in a fix-bed vertical quartz reactor, flowing H_2 for 1 h at 550°C. Subsequently, temperature was risen up to 700°C under N_2 atmosphere. Then CH_4 was flowed through the reactor for 3 h to proceed with its catalytic decomposition, yielding the carbon nanofibers (CNF). To obtain the Fe-MONW/CNF composites, equal amounts of MONW or Fe-MONW and CNF were placed in an agate vase with 7 agate balls (5 mm diameter), and 10 mL of ethanol, and ball-milled for 1 h at 100 rpm. The resulting mixture was dried overnight at 65°C.

2.2. Materials characterization

CNF, MONW, and Fe-MONW were fully characterized by several solid-state characterization techniques. Powder X-Ray Diffraction (XRD) was performed with a Bruker AXS D8 Advance diffractometer employing Cu Kα radiation and a θ–θ configuration. Crystal size was calculated by applying the Scherrer equation to the main peaks of the diffractogram. The determination of the crystallographic phases was carried out through Rietveld refinement. The morphology of MONW and CNF was investigated by both transmission (TEM) and scanning (SEM) electron microscopy. TEM images were acquired with a Tecnai F30 microscope operated at 300 kV. The samples were ultrasonically dispersed in ethanol for 15 min and then placed in a Cu carbon grid. SEM images were obtained with a Hitachi 3400-N microscope with the powdered samples directly placed on a carbon tape. Textural features of MONW were assessed through nitrogen physisorption at − 196°C in Micromeritics ASAP 2020. The amount of iron was determined by inductively coupled plasma combined with atomic emission spectrometry (ICP-AES) using an Xpectroblue-EOP-TI FMT26 spectrometer. This technique was also employed to determine the amount of nickel in the carbon nanofibers (CNF). In addition, the carbon and hydrogen content of CNF was determined by elemental analysis (EA) in a Thermo Flash 1112 analyzer (Thermoscientific Waltham). Finally, the chemical speciation of manganese oxides was determined by X-Ray photoelectron spectroscopy in an ESCA Plus Omicron spectrometer equipped with Mg (1253.6 eV) anode, 225 W (20 mA, 15 kV) power and using Casa XPS as software for the deconvolution of the peaks. Components were fitted with a Gaussian-Lorentzian (70%−30%) curve and a Shirley function was used for the baseline.

2.3. Electrochemical tests

The activity of MONW/CNF and Fe-doped MONW/CNF composites was investigated towards the critical reactions for the air electrode in an alkaline solution, *i.e.*, the oxygen reduction and the oxygen evolution reactions. The electrochemical experiments were carried out in a three-electrode cell, using a graphite rod as counter-electrode, a reversible hydrogen electrode as the reference electrode in the tests performed in KOH 0.1 M, and a Hg|HgO reference electrode in the tests performed in KOH 6 M. An ink composed of 5 mg of the catalyst under study, 10 μL of binder (Nafion solution 10 wt%., Alfa-Aesar), and 490 μL of ethanol (HPLC grade, Alfa Aesar) was prepared and deposited, drop by drop, on top of a rotating disk electrode (RDE), with a glassy carbon tip of 5 mm (diameter). A catalyst loading of 1018 μg cm^{-2} was obtained. The catalytic activity was assessed by applying linear sweep voltammetry (LSV) from 1.0 to 0.2 V *vs.* RHE to investigate the ORR, with a scan rate of 5 mV s^{-1} and varying rotating speeds from 400 to 2500 rpm and flowing O_2 in the electrolyte solution (0.1 M KOH, prepared from high-purity KOH, 99.99%, Alfa Aesar, and ultrapure water, Milli-Q, 18.2 MΩ cm). Before the ORR, LSV in nitrogen atmosphere was performed in the same potential range and used as baseline, subtracted to the oxygen-LSV. The OER was carried out with LSV from 1.0 to 1.9 V *vs.* RHE at the same scan rate and 1600 rpm of rotating speed to remove the evolved oxygen from the electrode. Endurance tests were carried out to investigate the stability of the catalysts, consisting in 50 cycles comprising 3 min at 1 mA cm^{-2} and 3 min at − 1 mA cm^{-2} at 1600 rpm rotation speed. Besides, a Gas Diffusion Electrode (GDE) was prepared by spray-coating a 1.6 cm diameter carbon paper piece with an ink of the same characteristics as the one of the RDE. A coverage of 0.71 mg cm^{-2} was achieved. Fifteen ORR-OER cycles of 5 h each and current densities of − 10 mA cm^{-2} and

10 mA cm^{-2}, respectively, were performed. The system of these tests used KOH 6 M as an electrolyte and a Hg|HgO reference electrode.

3. Results and discussion

3.1. Materials characterization

The chemical composition of carbon nanofibers was investigated with elemental analysis (EA) and inductive-coupled plasma spectroscopy (ICP). Carbon nanofibers contain solely carbon (89 wt%), hydrogen (1 wt%), and nickel (7.3 wt%, determined from ICP), from the CNF-growth catalyst. The high carbon content is consistent with what was observed during the growth of the CNF, as 300 mg of Ni:Cu:Al_2O_3 catalyst yielded approximately 3 g of CNF [36]. The chemical composition of manganese oxide nanowires was investigated by ICP, as shown in Table 1. MONW-120 and MONW-140 have almost identical compositions (58–59 wt% Mn and around 6 wt% K), indicating that the difference in the studied temperatures has a negligible impact on the composition of the nanowires. Potassium in the MONW comes from $KMnO_4$ employed during the synthesis. This potassium is present as K_2MnO_4 [35], so the amount of potassium correlates with the amount of manganese (VI), as will be discussed later. The total amount of Mn and K in the MONW nanowires is *ca.* 65%. Since no other elements are found in these materials, the amount of oxygen in the MONW can be determined (by difference), being *ca.* 35 wt%. Considering the stoichiometric formula of MnO_2, 36.8% is oxygen, close to 35% of our MONW. Fe-MONW show a lower Mn content (around 50 wt%), that decreases with increasing amount of iron, and more importantly, the K content decreases sharply, compared to the non-doped counterparts. Iron percentages in the Fe-MONW (2, 5.3, and 6.6 wt%) are close to the nominal loadings pursued (2, 5, and 7 wt%). These samples also show a higher amount of oxygen in their composition (calculated by difference): 39.6, 38.3, and 40.2 wt% in 2Fe-MONW-120, 5Fe-MONW-120, and 7Fe-MONW-120, respectively. This greater oxygen content can be related to their capacity to adsorb oxygen, as will be discussed in the next paragraphs, related to XPS analyses.

The chemical composition of MONW and Fe-MONW was also analyzed by XPS (Fig. S1 in Supporting Information). Table 2 reports the chemical composition of the MONW and Fe-MONW obtained from the deconvolution of the XPS spectra.

The elements found on the surface of the nanowires were O, Mn, K, and Fe. MONW-120 and MONW-140 differ in the amount of manganese and oxygen. The O:Mn atomic ratio is reported in Table 3, being 4:3 for MONW-120 and 3:1 for MONW-140. This significant difference could be explained by the adsorbed oxygen [37]. According to Xiao et al. [38], the synthesis of the nanorods at temperatures higher than 120 °C results in the "dissolution or etching of the extremes of the nanorods", slowly transforming them into nanotubes. In the high-resolution SEM images (Fig. S2a), we observed open ends in MONW-140, evidencing the dissolution/etching previously mentioned. These open ends could be responsible for the enhanced oxygen adsorption in MONW-140.

Potassium content determined by XPS (Table 2) ranges around 2–4 at % (corresponding to 3–6 wt% as shown in Table S1, being similar to the bulk content reported in Table 1). On the contrary, iron is found in excess on the surface of Fe-MONW (*ca.* 9–10 at% corresponding to 20 wt %, Table S1) compared to the bulk (see Table 1, from 2 to 6 wt%).

Iron-doped nanowires Fe-MONW present average O:Mn ratio around 6:1 and O:Me ratio (Me = Mn+Fe) of *ca.* 3.3:1, as reported in Table 3. This indicates that iron favours oxygen adsorption, as will be discussed later. Another interesting finding concerns iron concentration. 2Fe-MONW-120 has an atomic bulk concentration (reported in Table S2) of ~1 at% and a surface concentration of 8.9 at% (Table 2). 5Fe-MONW-120 with a bulk concentration of iron of 2.5 at%, presents a higher iron surface concentration, 10.4 at%. However, a further increase in the iron bulk concentration does not mean a further increase in the surface concentration, and consequently, 7Fe-MONW-120 has an iron surface concentration of 9.8 at%. These data suggest that iron tends to accumulate on the surface of the manganese oxide nanowires until a point of saturation. This is relevant since surface chemistry tends to affect catalytic processes severely.

The high-resolution spectra of the manganese 2p orbital are shown in Fig. 1**a** and Fig. S3**.** The Mn peak shows two $2p_{3/2}$ components: one around 642.0 eV, ascribed to MnO_2 (Mn (IV)) and one around 644.3 eV, ascribed to K_2MnO_4 (Mn (VI)). Biesinger et al. reported that pure MnO_2 samples show a peak at lower binding energy, corresponding to Mn (III), which is not observed in our samples [39]. This fact, together with the presence of Mn (VI), means that the reduction of $KMnO_4$ during the synthesis is incomplete. The amount of Mn (VI) on the surface is consequently related to the amount of potassium, as can be seen in 5Fe-MONW-120 (Fig. 1c) and 7Fe-MONW-120 (Fig. S3c), having a lower concentration of both surface potassium (around 2 at%, Table 2) and Mn (VI) (around 7–9 at%).

The analysis of the O 1s orbital allows the identification of the oxygen species present on the surface of the nanowires (Figs. 1b and 1d, and Fig. S4). Two peaks were identified: one at ~529.5 eV, corresponding to lattice oxygen – either bond to Mn or Fe (peaks of manganese and iron oxide appear at almost the same binding energy [40]) and, another one around 531.1 eV, which corresponds to adsorbed oxygen, OH^- groups or oxygen vacancies [41] (Fig. 1b). Since samples with a larger oxygen content also have a more significant oxygen surface content, it is fair to assume that this peak at around 531.1 eV is in fact adsorbed oxygen. Following this idea, the lattice to adsorbed oxygen ratio is higher in MONW-120 than in MONW-140 – 65:35 and 57:43, respectively –, which helps to explain the observed difference in the manganese to oxygen ratio observed in these samples. The amount of adsorbed oxygen in the Fe-MONW is even higher, with a 50:50 ratio of lattice to adsorbed oxygen ratio in the three iron-doped manganese

Table 1
Elemental composition determined by ICP-OES of the synthesized materials.

Material	wt%			
	Manganese	Iron	Nickel	Potassium
CNF	-	-	7.3	-
MONW-120	58	-	-	6.1
MONW-140	59	-	-	6.7
2Fe-MONW-120	52	2.0	-	6.4
5Fe-MONW-120	53	5.3	-	3.4
7Fe-MONW-120	51	6.6	-	2.2

Table 2
Surface composition of the synthesized materials measured by XPS.

Material	Atomic %			
	O	Mn	Fe	K
MONW-120	55.2	41.9	-	2.9
MONW-140	72.1	23.5	-	4.4
2Fe-MONW-120	74.1	13.1	8.9	3.9
5Fe-MONW-120	74.9	12.5	10.4	2.2
7Fe-MONW-120	75.3	13.0	9.8	1.9

Table 3
O:Mn atomic ratio in the bulk (determined from ICP) and on the surface (determined from XPS).

Material	O:Mn bulk ratio	O:Mn surface ratio	O:Me surface (Me = Mn+Fe)
MONW-120	2.1:1	4:3	4:3
MONW-140	2:1	3:1	3:1
2Fe-MONW-120	2.6:1	5.7:1	3.4:1
5Fe-MONW-120	2.5:1	6:1	3.3:1
7Fe-MONW-120	2.7:1	5.8:1	3.3:1

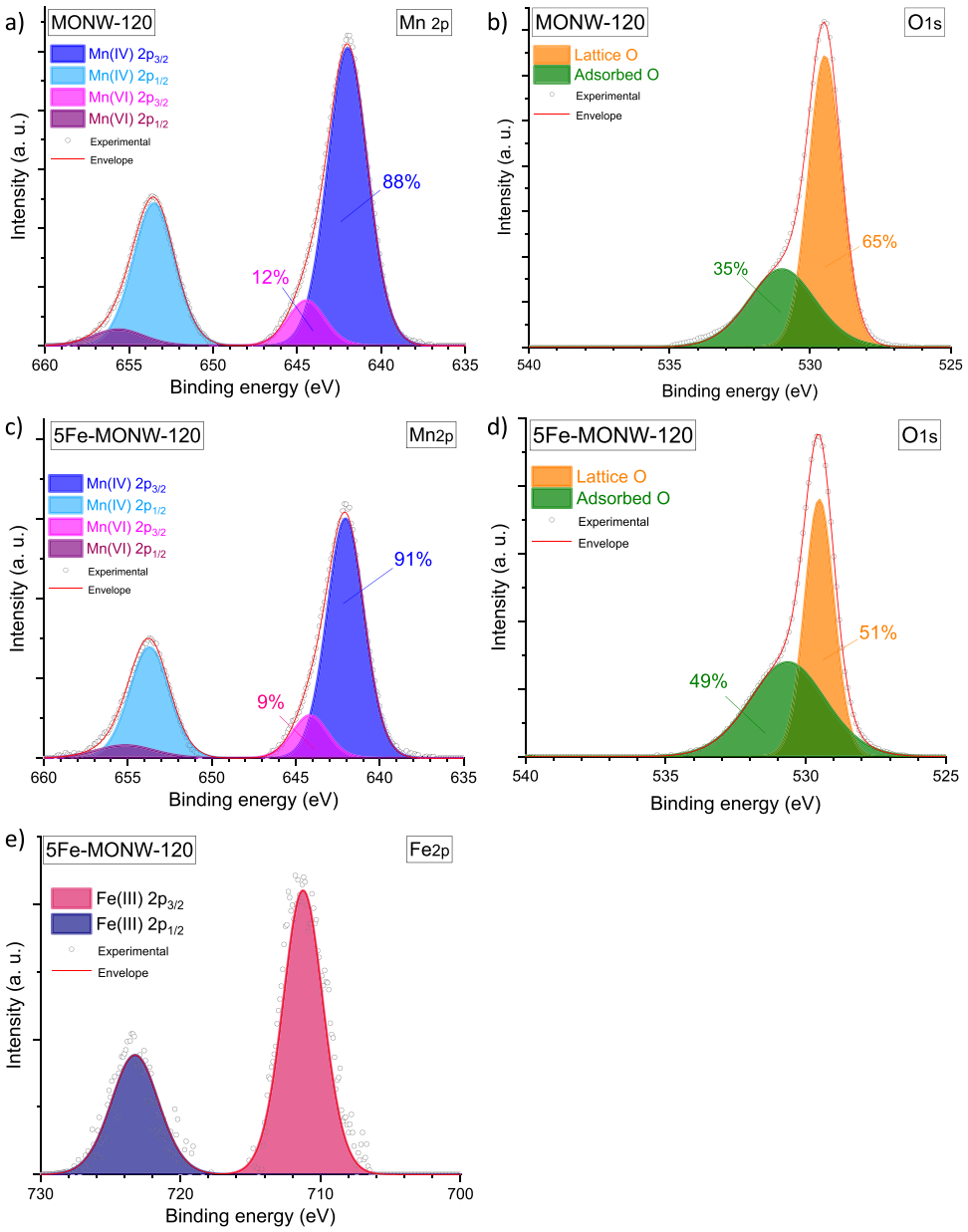

Fig. 1. High-resolution XPS spectra of orbitals a) Mn 2p and b) O 1s, in MONW-120; c) Mn 2p, d) O 1s and e) Fe 2p, in 5Fe-MONW-120. Baseline subtracted in all the spectra.

oxide nanowires (Fig. 1d and Fig. S4). In iron-containing samples, the Fe 2p orbital was also analyzed (Fig. 1e and Fig. S5). The position of the main iron peaks in 2Fe-MONW-120, 5Fe-MONW-120, and 7Fe-MONW-120 at around 711.5 eV allows us to infer that the iron species has a + 3 oxidation state, such as Fe_2O_3 or FeOOH [40]. The lack of a satellite peak between the $2p_{3/2}$ and $2p_{1/2}$ components and the gap between them of approximately 12.5 eV is similar to the goethite XPS spectrum [42]. These Fe^{3+} ions create oxygen vacancies in the MnO_2 lattice, which can enhance the catalytic activity of MnO_2 towards ORR, as reported by Li et al. [43].

XRD studies revealed the crystalline structures of the MnO_2 nanowires (Fig. 2). The only crystalline phase observed, obtained applying Rietveld refinement, was α-MnO_2 (JCPDS: 00–044–0141) confirming that iron ions are inserted in the manganese oxide lattice.

The addition of iron diminishes the size of the MnO_2 crystallite, increasing the number of defects, as reported in Table 4. This can be deducted from the progressive widening of the diffraction peaks with increasing amounts of iron (Fig. 2), particularly appreciable at the (211) peak at 37°. It must be remarked that the inclusion of Fe ions in the α-MnO_2 structure is not reflected as a shift of the peak position in the diffractogram. The similar ionic radius of Fe^{3+} and Mn^{4+} (73 and 67 pm, respectively [44]) means that interplanar distances are not significantly modified, and Bragg angles do not change. The defects induced in the lattice by ferric ions are related to oxygen vacancies due to their lower charge with respect that of Mn^{4+} ions. Thse defects are not caused by the strain ascribed to the different size between ions.

From the crystallite size values, the dislocation density (δ) can be calculated by applying Eq. (1), also reported in Table 4. The dislocation density increases with increasing iron content. The dislocation density represents the concentration of defects in a crystal and is defined as the length of dislocation lines per volume [44,45]:

$$\delta = \frac{1}{D^2} \quad (1)$$

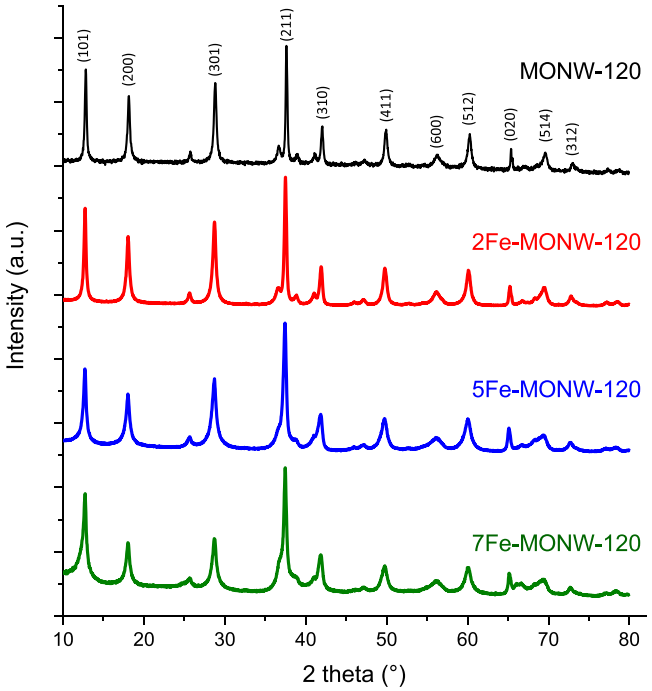

Fig. 2. XRD pattern of manganese oxide nanowires and iron-doped manganese oxide nanowires synthesized at 120°C. Miller indexes for α-MnO_2 are referenced within the figure [47,48].

Table 4
XRD parameters (crystal size and dislocation density).

Material	Crystallite size / nm	Dislocation density / 10^{-4} nm^{-2}
MONW-120	37.0	7.3
2Fe-MONW-120	23.3	18.4
5Fe-MONW-120	16.1	38.6
7Fe-MONW-120	14.6	46.9

XRD pattern was also obtained for CNF (Fig. S6a), where the only observable crystalline phases are graphitic carbon and metallic nickel. Highly graphitic carbon nanofibers are good electrical conductors and can enhance electrochemical reactions [46].

The textural properties of CNF, MONW and MONW/CNF composites were studied by nitrogen physisorption at 77 K (Fig. S7, and Table S3). Carbon nanofibers show a BET surface area of 94 m^2 g^{-1} in accordance with previous studies [49,50]. In the case of the MONW, the synthesis temperature does not have a significant effect on the textural properties, as MONW-120 and MONW-140 present surface area values of 23 m^2 g^{-1} and 24 m^2 g^{-1}, respectively. Doping with iron did not significantly affect the textural properties of MONW. Fe-MONW presented surface area values in the same range (20–26 m^2 g^{-1}) as their non-doped counterparts.

SEM and TEM images of the composites show the morphology of both CNF and MONW (Fig. 3). Carbon nanofibers have a fishbone structure, as ascertained from Fig. 3a, and diameters around 50 nm, as appreciated in Fig. 3b. Fig. 3c shows a bunch of MONW, highly cross-linked, with a needle-like shape. Fig. 3d shows an image at higher magnification of an isolated MONW, with *ca.* 35 nm diameter and from 50 to 100 nm long. TEM images of the composite (Figs. 3e and 3f) show a good contact between the manganese oxide and the carbon phases, which is essential, as will be discussed in the next section. No iron particles were detected in the HR-TEM of the Fe-MONW, which confirms that iron is embedded in the MnO_2 lattice. Figs. 3g and 3h show the particle size distribution for the MONW-120 in terms of both nanowire diameter (Fig. 3g) and nanowire length (Fig. 3h). The statistical distribution was obtained by measuring over 130 nanowires. The average nanowire diameter is around 75 nm, whereas the length is usually around 100 nm. In addition, no significant morphological differences were observed between the nanowires synthesized at 120 °C or 140 °C, as shown in Figs. S2b and S2c.

3.2. Electrochemical characterization

3.2.1. Activity towards oxygen reduction and evolution reactions

The performance of the catalysts towards ORR and OER was assessed by linear sweep voltammetry (Fig. 4a). The onset potentials for ORR (E_{ORR}) and OER (E_{OER}) were calculated as the potential when the current density reaches − 0.1 mA cm^{-2} and 1 mA cm^{-2}, respectively. Based on these values, the onset overpotentials for ORR (η_{ORR}) and OER (η_{OER}), reported in Fig. 4b, were also calculated taking into consideration the standard O_2 reduction potential, 1.23 V. Another important parameter to assess the performance of these bifunctional catalysts is the reversibility gap, ΔE, also reported in Fig. 4b. This value is fundamental for the performance of the final metal-air battery device, since it directly influences the faradaic efficiency. ΔE is usually defined as the difference between the potential at which OER reaches 10 mA cm^{-2} (E_{10}) and the half-wave potential for the ORR (E_{HWP}). This will be the one used in this manuscript. Other works in the literature report ΔE as the difference between the potential for the OER at 10 mA cm^{-2} and the potential for the ORR at − 1 mA cm^{-2} [34,51].

MONW-120/CNF composite catalyst was tested against the CNF and MONW (Fig. 4a). The polarization curves show a synergistic effect between the manganese oxide nanowires (MONW) and the carbon nanofibers (CNF), which is especially notorious in ORR. MONW/CNF composites show an onset potential shifted towards more positive values with respect the CNF (70 mV shift) and a higher limiting current density (−5 mA·cm^{-2} for the composite *versus* −4 mA·cm^{-2} for the individual components). On the other hand, CNF and MONW-120/CNF composite show almost the same behaviour for the OER. CNF have a 7.3 wt% of nickel in their composition, responsible for the catalytic activity towards the OER. To confirm this, carbon nanofibers were leached with hot hydrochloric acid (2 h, 60 °C, under sonication) and tested again for ORR and OER (see LSV in Fig. S8 in the supporting information). Acid-leached CNF has a slightly lower activity towards both ORR and OER with respect to the pristine CNF. Thus, the onset potential for the OER for acid-leached CNF shifts more than 50 mV and for ORR more than 25 mV *versus* CNF, due to the presence of the catalytically active nickel particles.

Fig. 4b shows the reversibility gap *(left Y axis)* and the onset overpotentials for both the ORR and OER *(right Y axis),* confirming the synergistic effect of the CNF with the MONW-120. It is evident that the MONW/CNF composites have lower ΔE gaps than the individual phases (CNF or MONW), mainly due to the poor activity of CNF towards ORR and of MONW towards OER.

The number of electrons transferred during the ORR was calculated applying the Levich equation (Eq. 2) to the polarization curves:

$$j_L = 1.95nFAC^*_{O_2}D^{1.5}_{O_2}\nu^{-1/6}f^{-0.5} \quad (2)$$

Where j_L is the current density at the diffusional limit (E = 0.2 V *vs.* RHE), n is the number of electrodes transferred (2 for oxygen reduction to H_2O_2 and 4 to OH^-), F is the Faraday constant (96485 C/mol), A is the area of the electrode (0.196 cm^2), $C^*_{O_2}$ is the saturation concentration of oxygen in the electrolyte (1.21 mol m^{-3}), D_{O_2} is the diffusivity of oxygen in the electrolyte (1.87 * 10^{-9} m^2 s^{-1}), ν is the cinematic viscosity of the electrolyte solution (10^{-6} m^2 s^{-1}) and f is the rotation frecuency of the electrode, in Hz. The ORR goes through a mechanism of 2.7 electrons for MONW-120 and 2.9 electrons for the CNF. In the composites (MONW/CNF), the number of electrons increases up to 3.4 for MONW-120/CNF and 3.5 for MONW-140/CNF. These increase in the number of electrons confirms the synergistic effect between the MONW and the CNF. The

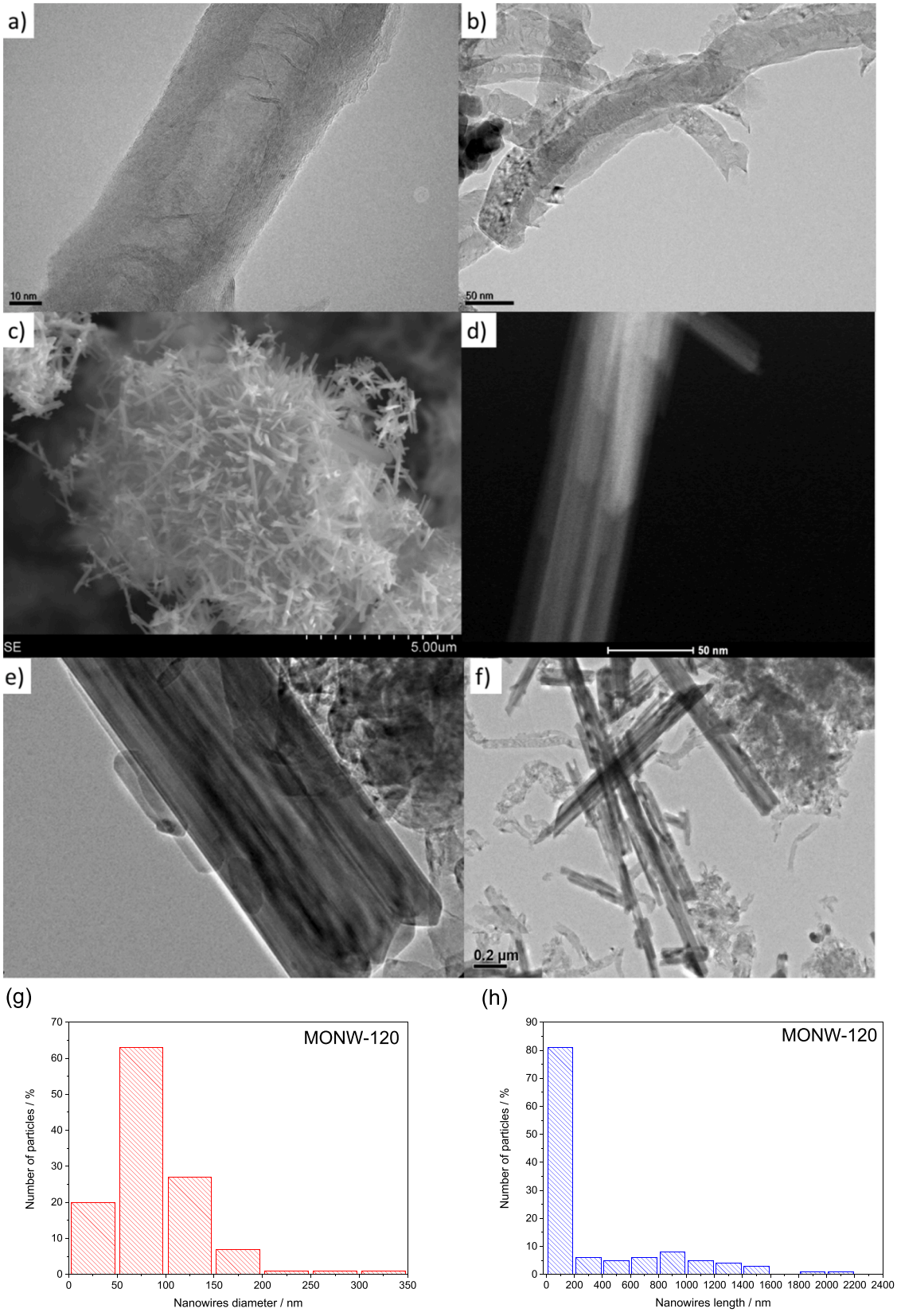

Fig. 3. a) HR-TEM image of a single carbon nanofiber. b) TEM image of carbon nanofibers. c) SEM image of MONW-120. d) STEM image of a single manganese oxide nanowire (MONW-120). e) TEM image of the composite MONW-120/CNF and f) TEM image of the composite 5Fe-MONW-120/CNF, g) Particle size distribution for MONW-120 in terms of the average nanowire diameter and h) Particle size distribution for MONW-120 in terms of the average nanowire length.

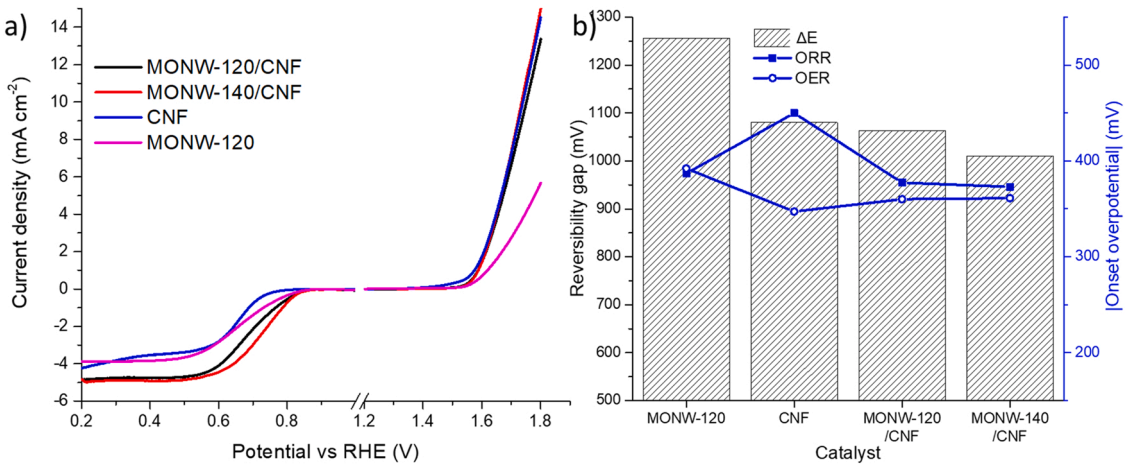

Fig. 4. a) Polarization curves of the MONW/CNF composites, CNF and MONW materials, in a RDE at 1600 rpm in KOH 0.1 M. b) Summary of the performance of the catalysts in terms of overpotential towards OER/ORR and reversibility gap, ΔE.

textural properties of the carbon nanofibers provide a surface where oxygen can be adsorbed and then reduced. In any case, the number of electrons for our catalysts are lower than the theoretical maximum of 4 – achieved by the benchmark Pt/C catalyst – but still means than 75% of the oxygen reduction occurs *via* the hydroxide intermediate and only 25% *via* the peroxide route. These results were corroborated by applying the Levich equation to different rotation speeds (Fig. S9 and Fig. S10).

Tafel slopes (m_T) at low current density (<2 mA cm^{-2}) and exchange current densities (j_0) were also obtained in order to compare the catalysts and gain insight into the mechanisms of the reactions. To obtain the kinetic current density – *i.e.,* the intrinsic current density – the Koutecky-Levich approach was used (Eq. 3):

$$\frac{1}{j} = \frac{1}{j_k} + \frac{1}{j_L} \tag{3}$$

Where j is the observed current density (after subtracting the background) and j_k is the kinetic current density to be determined.

Fig. 5**a** shows the Tafel plots for ORR, that range between 53 and 134 mV dec^{-1}, with MONW-120/CNF presenting the lowest value. The benchmark catalyst, Pt/C, has a higher slope of 84 mV dec^{-1}, but also a much higher exchange current density of 4.2 * 10^{-4} mA cm^{-2} against the 9.1 * 10^{-9} mA cm^{-2} of the catalyst MONW-120/CNF. The synergistic effect between CNF and MONW is also reflected in their Tafel slope values, 76 mV dec^{-1} for the CNF and 134 mV dec^{-1} for the MONW, with respect to the MONW/CNF composite presenting 53 mV dec^{-1}.

According to the literature [17,52–54], the fundamental steps ascribed to the reduction of oxygen in alkaline media are the following:

$$M + O_2 \rightleftharpoons MO_2 \tag{4}$$

$$MO_2 + e^- \rightleftharpoons MO_2^- \tag{5}$$

$$MO_2^- + H_2O \rightleftharpoons MO_2H + OH^- \tag{6}$$

$$MO_2H + e^- \rightleftharpoons MO + OH^- \tag{7}$$

$$MO + H_2O + e^- \rightleftharpoons MOH + OH^- \tag{8}$$

$$MOH + e^- \rightleftharpoons M + OH^- \tag{9}$$

M is an adsorption site in the catalyst. According to Shinagawa et al. [55], when the second step (Eq. 5) is the rate-determining step (RDS), a Tafel slope of 120 mV dec^{-1} should be expected. The Tafel slope for ORR in the material MONW-120 is 134 mV dec^{-1}, so it is a fair assumption that the semi-reaction from Eq. 5 is the rate-determining step over manganese nanowires. Taking a closer look at Eq. 5, a more significant amount of adsorbed oxygen (MO_2) should increase its rate, so materials with a higher ability to adsorb oxygen would yield faster ORR. This might explain why MONW-140/CNF has a better half-wave potential for the ORR than MONW-120/CNF, even though they have similar onset potentials. As was shown in the previous section, MONW-140 has a better ability to adsorb oxygen than MONW-120. The 53 mV dec^{-1} slopes of composites MONW-120/CNF suggest that reaction (7) could be the RDS, as a 40 mV dec^{-1} followed by a 120 mV dec^{-1} is expected when

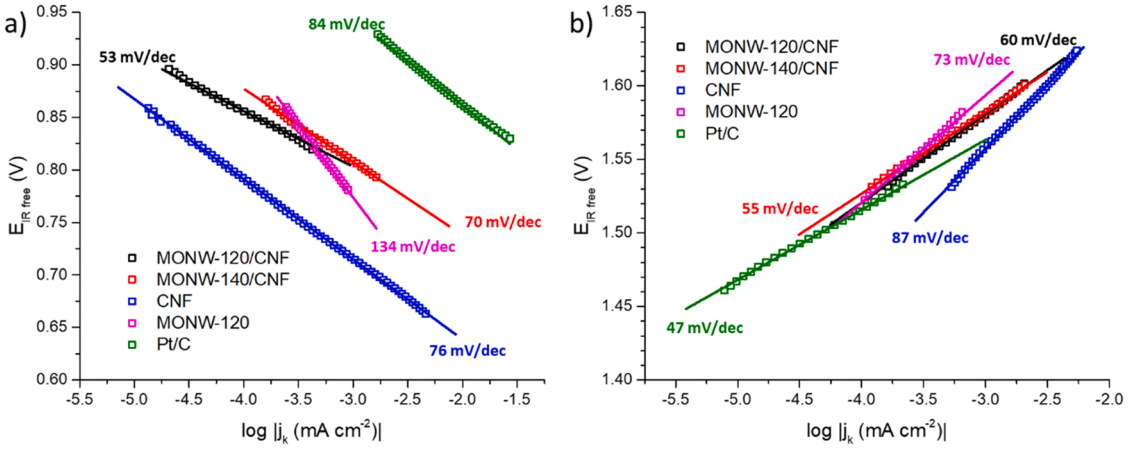

Fig. 5. Tafel plots for a) ORR and b) OER for CNF, MONW-120 and MONW/CNF-composites.

this is the case. Electrochemical Impedance Spectra (EIS) studies were carried out to gain a deeper insight about the RDS of ORR. See Fig. S11 in Supporting Information.

Fig. 5**b** shows the Tafel slope for the OER. The benchmark IrO_2 catalyst has a notably superior performance with a value of 47 mV dec^{-1}, while composites MONW-120/CNF and MONW-140/CNF show slopes of 60 and 55 mV dec^{-1}, respectively. In this reaction, the synergistic effect is less evident but still observable, as the Tafel slopes of CNF and MONW-120 are similar (73 and 87 mV dec^{-1} respectively), but slightly higher than those of the composites. As previously stated, nickel on CNF is active for the OER. MONW shows poorer electrochemical activity than CNF in the polarization curves and a lower Tafel slope. This is explained by the higher exchange current density of CNF, 1.7 * 10^{-4} *versus* MONW-120, 1.0 * 10^{-5} mA cm^{-2}, mainly due to the larger surface area of the CNF.

The commonly accepted route for oxygen evolution in alkaline electrolyte is the following:

$$M + OH^- \rightleftharpoons MOH + e^- \quad (10)$$

$$MOH + OH^- \rightleftharpoons MO + H_2O + e^- \quad (11)$$

$$MO + OH^- \rightleftharpoons MOOH + e^- \quad (12)$$

$$MOOH + OH^- \rightleftharpoons MOO^- + H_2O \quad (13)$$

$$MOO^- \rightleftharpoons M + O_2 + e^- \quad (14)$$

According to the same study cited before [55], a Tafel slope of 40 mV dec^{-1} followed by a higher slope of around 120 mV dec^{-1} – as the one obtained with IrO_2 – is a sign of reaction 12 being the OER rate-determining step. The slopes obtained with the rest of the catalysts, around 60 mV dec^{-1} followed by a higher slope at higher overpotentials, imply that the fourth step (reaction 13) is the rate-determining step.

Due to the close results obtained with MONW-120/CNF and MONW-140/CNF and their interesting electrochemical behaviour, iron-doped manganese oxide nanowires were synthesized at 120 °C and then mixed with CNF to obtain iron-doped composites, Fe-MONW-120 (Fig. 6).

Doping with iron has a beneficial effect on the activity of the composites, since all Fe-MONW-120/CNF composites show superior activity to both reactions in terms of onset potential and current density. The number of exchanged electrons, obtained from K-L plots, does not change upon doping, in comparison to MONW/120-CNF, being 3.4 for all the iron-doped composites. As previously stablished in Section 3.1, iron-doped manganese oxide nanowires have defects, mainly oxygen vacancies, that act like active sites for ORR and OER. These defects are also responsible for the enhanced capacity to adsorb oxygen and OH^-, which is crucial for oxygen reduction [25]. The catalyst with a 5 wt% Fe shows the best activity for both ORR/OER with the lowest onset overpotential and, the lowest ΔE value, 922 mV. ΔE is 140 mV lower compared to the non-doped counterpart (MONW-120/CNF), corroborating the outstanding effect of doping with iron in the electrochemical activity. 5Fe-MONW-120 presents the highest iron surface concentration among the three iron-doped nanowires. Besides, it has a similar amount of defects to 7Fe-MONW-120, but a slightly higher surface area, which are sufficient to enhance the catalytic activity of 5Fe-MONW with respect other samples.

Benchmark catalysts are not bifunctional, Pt/C is not a good catalyst for the OER and IrO_2 is not active for the ORR. For this reason, they were tested independently for their corresponding reactions, and ΔE was not determined. Taking this into account, the differences in activity of benchmark materials with our catalysts were compared in terms of onset overpotential for ORR and OER, and E_{hw} for the ORR. For the OER, 5Fe-MONW-120/CNF and 7Fe-MONW-120/CNF have onset overpotentials practically equal to IrO_2 (only 5 and 3 mV higher) . On the other hand, for the ORR, 5Fe-MONW-120/CNF and 7Fe-MONW-120/CNF present onset overpotentials 147 mV and 155 mV higher than Pt/C, as expected, since Pt/C is an excellent catalyst for the ORR. It must be noted that the number of exchanged electrodes– calculated by Koutecky-Levich equation – does not significantly change in the Fe-MONW/CNF catalysts. This suggests that iron in the manganese structure does not change the mechanism of the reaction but somewhat changes the activation energy of the steps of oxygen reduction.

Table 5 compares all the previously cited electrochemical parameters for ORR and OER over each catalyst. The difference between the composites for ORR is more evident when comparing the half-wave potentials. These values are 687, 736, 765, and 735 mV for MONW-120/CNF, 2Fe-MONWFe-120/CNF, 5Fe-MONW-120/CNF, and 7Fe-MONW-120/CNF, respectively. 5Fe-MONW-120/CNF presents a half-wave potential 30 mV more positive than 7Fe-MONW-120/CNF. This is also the case when comparing the E_{hwp} of 5Fe-MONW-120/CNF *versus* Pt/C, presenting a difference of 110 mV

Tafel slopes were also obtained for the iron-doped composites (Fig. 7). For ORR, the four composites show similar Tafel slopes, with the undoped composite having the lowest one, 53 mV dec^{-1}. On the other hand, 5Fe-MONW120/CNF – the most active composite for ORR – has a slightly higher Tafel slope, 68 mV dec^{-1}, but an exchange current density 1.8 * 10^{-6} mA cm^{-1}, two orders of magnitude higher than the non-doped composite and two orders of magnitude lower than the Pt/C

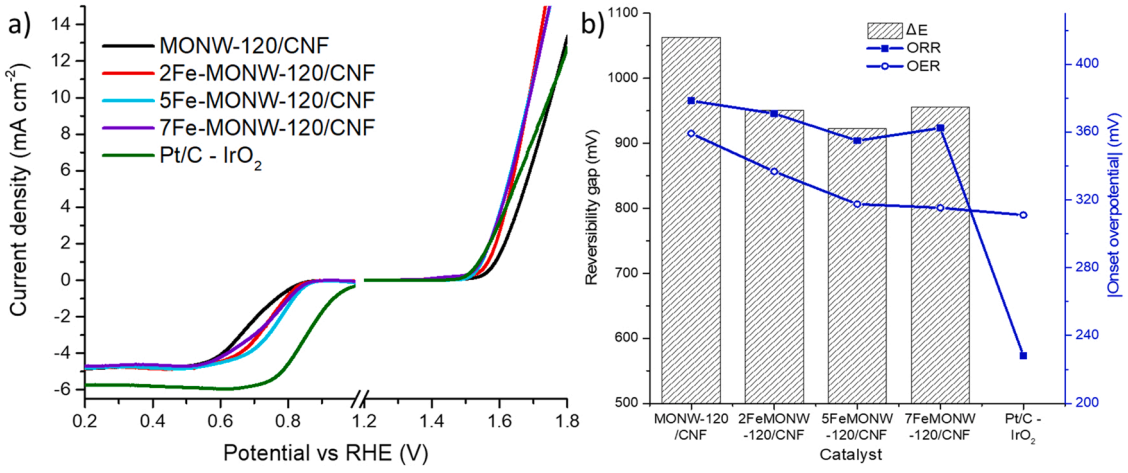

Fig. 6. a) ORR-OER polarization curves of the iron-doped MONW/CNF composites, in a RDE at 1600 rpm in KOH 0.1 M. b) Summary of the performance of the catalysts in terms of overpotential towards OER/ORR and reversibility gap, ΔE. Benchmark catalysts are also included for the sake of comparison: Pt/C for the ORR, and IrO_2 for the OER.

Table 5
Electrochemical parameters obtained from Figs. 4, 5, 6 and 7 for all the tested catalysts.

Catalyst	Oxygen Reduction Reaction						Oxygen Evolution Reaction				ΔE (V)
	E_{hwp} (V *vs.* RHE)	η_{ORR} (mV)	j_L (mA cm^{-2})	*n*	$j_{0,ORR}$ (mA cm^{-2})	$m_{T,ORR}$ (mV dec^{-1})	E_{10} (V *vs.* RHE)	η_{OER} (mV)	$j_{0,OER}$ (mA cm^{-2})	$m_{T,OER}$ (mV dec^{-1})	
CNF	0.66	450	4.2	2.9	1.8 * 10^{-10}	76	1.74	347	1.7 * 10^{-4}	87	1.08
MONW-120	0.66	387	3.9	2.7	4.9 * 10^{-10}	134	1.90	392	1.0 * 10^{-5}	73	1.24
MONW-120/CNF	0.69	377	4.8	3.4	9.1 * 10^{-9}	53	1.75	360	1.4 * 10^{-6}	60	1.06
MONW-140/CNF	0.73	373	4.9	3.5	8.1 * 10^{-7}	70	1.74	361	4.2 * 10^{-7}	55	1.01
2Fe-MONW-120/CNF	0.74	371	4.8	3.4	2.4 * 10^{-7}	63	1.69	331	1.1 * 10^{-6}	55	0.95
5Fe-MONW-120/CNF	0.77	355	4.8	3.4	1.8 * 10^{-6}	68	1.69	317	8.5 * 10^{-7}	51	0.92
7Fe-MONW-120/CNF	0.73	362	4.8	3.4	4.0 * 10^{-6}	74	1.69	315	1.3 * 10^{-5}	63	0.96
Pt/C – IrO_2	0.88	208	5.7	4.0	4.2 * 10^{-4}	84	1.75	312	1.0 * 10^{-7}	47	-

E_{hwp} = Half-wave potential;; η_{ORR} = onset overpotential for the ORR (difference between the standard reduction potential and the potential at which ORR reaches −0.1 mA cm^{-2}); j_L = limiting current density; n = number of exchanged electrons; i_0 = exchange current density, $m_{T,ORR}$ = Tafel slope for the ORR; E_{10} = potential at 10 mA cm^{-2}; η_{OER} = onset overpotential for the OER (difference between the potential at which OER reaches 1 mA cm^{-2} and the standard reduction potential); $m_{T,OER}$ = Tafel slope for the OER. ΔE = reversibility gap, calculated as $E_{10} - E_{hwp}$.

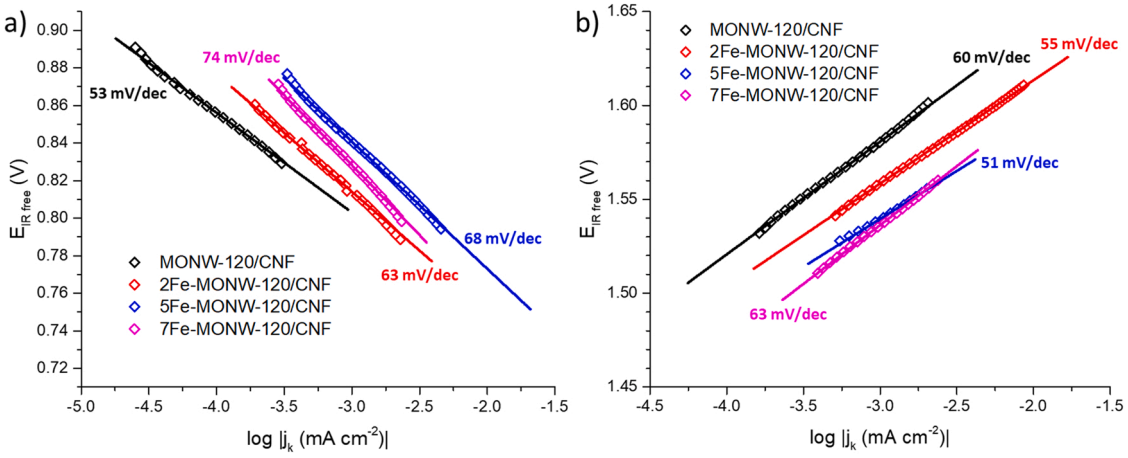

Fig. 7. Tafel plots for a) ORR and b) OER of the iron-doped MONW/CNF composites.

catalyst. There is a trend between the amount of iron and the Tafel slopes, with the slope increasing with the iron percentage, up to 74 mV dec^{-1} in the 7% iron composite. The Tafel slopes for the oxygen evolution show even less variability, with the composite 5Fe-MONW-120/CNF exhibiting a slope very close to that of the benchmark catalyst, 51 mV dec^{-1}. Only 12 mV dec^{-1} of difference separates the Tafel slopes of this catalyst and that of the most active composite OER, 7Fe-MONW-120/CNF. The latter, however, has one order-of-magnitude higher exchange current density, 1.3 * 10^{-5} against 8.5 * 10^{-7} mA cm^{-2}. These values are similar to what is found in literature, where values around 60 mV dec^{-1} are generally observed for OER over Mn catalysts [35,56,57].

A comparison between our best catalyst (5Fe-MONW-120/CNF) and several reported catalysts in the literature is presented in Table 6. Catalysts based on similar formulations, employing both manganese and carbon and other catalysts based on non-critical materials have been selected (only studies performed in KOH 0.1 M were included). Our catalyst performs relatively well in terms of reversibility against this kind of materials, as ΔE in literature ranges from 0.71 to 1.20 V. Catalysts obtained by Zhan et al. [58] and by Ma et al. [59], for example, show a reversibility gap of 0.85 V. However, those materials include the synthesis of graphene oxide by Hummer's method and the use of formamide, respectively, with the economical, practical and environmental concerns associated to those methods. The catalyst with the lowest reversibility gap we found in the literature [60], on its side, uses reagents like dioxane in its synthesis, with similar issues. Other Mn-based catalyst with low ΔE rely on the use of cobalt-based formulations, that are not desirable either.

3.2.2. *Stability tests*

Accelerated degradation endurance tests were performed to screen the durability of the best catalyst 5Fe-MONW-120/CNF over cycling (Fig. 8). The tests were carried out over the same RDE at 400 rpm, with negative and positive current densities of 1 mA cm^{-2}. The test comprised 50 cycles of 3 min charging (OER) and 3 min discharging (ORR). At the beginning, the estimated overpotentials for OER (η_{OER}) and ORR (η_{ORR}) are 317 and 418 mV, and the reversibility gap is 735 mV, in accordance with the one calculated from the polarization curve in Fig. 6. The OER overpotential slowly increases from 317 to 331 mV in the 50th cycle. The ORR, on its side, showed a decrease in the potential by cycle 27, having an average overpotential increase of 12 mV over the entire test. Adjusting linear models to the change in

Table 6
Comparison between electrochemical parameters for the best catalyst in this work and non-critical-materials catalysts found in literature.

Catalyst	Ref.	E_{hwp} (V *vs.* RHE)	E_{10} (V *vs.* RHE)	ΔE (V)
5Fe-MONW-120/CNF	**This work**	**0.77**	**1.69**	**0.92**
$MnCo_2O_4$@C	[61]	0.80	1.66	0.89
Electronic and defective $CaMnO_3$ nanotubes	[62]	0.76	1.70	0.94
Iron-doped manganese oxide nanorods	[35]	0.69	1.89	1.20
Single Fe atom on S, N-Codoped Nanocarbon	[63]	0.84	1.64	0.80
Ni-Fe layer double hydroxide @ rGO	[58]	0.63	1.48	0.85
Atomically dispersed Fe *via* Ni neighbouring	[59]	0.84	1.69	0.85
Fe/Ni dual-active sites anchored in honeycomb porous carbon material	[64]	0.87	1.59	0.71
N-doped graphene with topological defects	[65]	0.78	1.71	0.93
N, S co-doped oxygen-functionalized Vulcan XC/72	[66]	0.81	1.58	0.77
NiO-Mn_2O_3-carbon dots catalyst	[67]	0.84	1.53	0.69
Mn-Fe-Ni oxides supported on multiwall carbon nanotubes	[68]	0.81	1.57	0.76
Ni|MnO interfaces over carboxylic-functionalized carbon nanofibers	[69]	0.83	1.58	0.75
Manganese MOF @reduced graphene oxide nanocomposite	[70]	0.98	1.84	0.86
Ultrahin amorphous MnO_2-C (prawn shell derived)	[71]	0.97	1.59	0.77

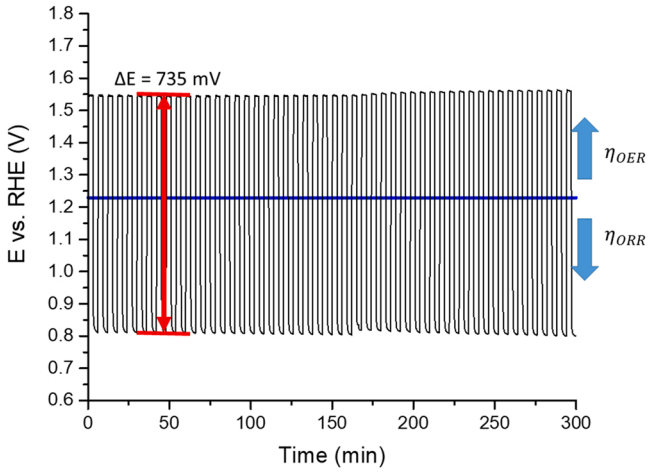

Fig. 8. a) Chronopotentiometric cycles over catalyst 5Fe-MONW-120/CNF. Test carried out at ± 1 mA cm^{-2} for 3 min for each reaction.

overpotential, in average, the OER overpotential increases 0.26 mV per cycle and the ORR overpotential increases 0.10 mV per cycle, evidencing that 5Fe-MONW-120/CNF shows a really stable behavior.

Long endurance tests, shown in Fig. 9, at higher current densities were performed in GDE to test the catalyst under more demanding and realistic conditions, namely, ± 10 mA cm^{-2} for both OER and ORR and 2.5 h for each reaction. For the first four cycles (20 h of operation), 5Fe-MONW-120/CNF shows a reasonably stable behavior, with the overpotentials for both OER and ORR increasing very slowly. However, at the end of the fourth oxygen reduction cycle, a significant increase in the overpotential – manifested as a sharp fall (for the ORR) and increase (for the OER) of the measured potential – is appreciated. After this sudden change, the overpotential for ORR increases slowly but steadily. In contrast, the overpotential for OER stays constant until the fourteenth-fifteenth cycle when another sharp increase can be seen. This sharp variation of the potential can be due to the excessive formation of oxygen bubbles, partially covering the electrode area, which could affect to the measuring of the potential with respect to the reference potential. This could entail a higher applied current to the electrode, eventually causing a higher electrode degradation. As a result, for the first four cycles (first 20 h of operation), the reversibility gap **(**Fig. 9**b)** stays below 850 mV, reaching 950 mV during cycles 5–13 and exceeding 1000 mV after. The combination of a sudden but sharp loss of activity (*e.g.,* between cycles 4 and 5) and a sustained but slower deactivation suggests two different deactivation causes or mechanisms acting simultaneously. Post-mortem XRD analysis was performed in the GDE electrode to investigate if a change in the crystalline phases of the electrode could be responsible for the deactivation of the electrode **(**Fig. S12**).** No change in the crystal phases, crystallinity, or crystal size could be observed, so the formation of bubbles in the electrode, affecting the reference potential, could explain the deactivation, as previously mentioned.

4. Conclusions

Bifunctional easy-synthesis oxygen catalysts composites based on iron-doped (2–7% wt.) manganese oxide nanowires (Fe-MONW) and carbon nanofibers (CNF) were tested as electrodes for alkaline oxygen evolution (OER) and reduction (ORR) reactions. The Fe-MONW/CNF composites show an enhanced activity compared to their individual phases (CNF and MONW) and onset potentials similar to the benchmark catalysts, especially for OER. Doping with iron reduced the onset overpotential for both ORR and OER, leading to a decrease in the reversibility gap of *ca.* 140 mV, reaching as low as 922 mV. The overpotential for OER decreased monotonically with the amount of iron in the studied range, while the overpotential for ORR reached an optimal at 5% wt. Physical-chemical characterization determined that iron creates vacancies in the MnO_2 lattice, which increases its catalytic activity by favoring the adsorption of oxygen. The analysis of the Tafel slopes reveals that combining CNF and MONW changes the rate-determining step of the reaction. However, this does not occur by doping MONW with iron (Tafel slopes do not change significantly). Endurance tests were also carried out with mild and challenging conditions for the 5Fe-doped MONW/CNF composite, which presented remarkable stability, with a stable potential for over 20 h, keeping the reversibility gap around 800 mV, which is an outstanding result, taking into account the higher current density employed (more challenging conditions).

The synergy between the iron-doped manganese nanostructure and the carbon nanofiber leads to a remarkable reversibility and enhanced performance for the oxygen reduction (ORR) and evolution (OER) reactions, along with a remarkable stability, a key issue for the future implementation of this kind of devices.

CRediT authorship contribution statement

N.I. Villanueva-Martínez is responsible for the investigation, conducting the research and investigation process, specifically performing the experiments, and data collection. Also N.I. Villanueva-Martínez is responsible for data curation and writing of the draft. C. Alegre is responsible for the conceptualization, planning and execution of the research activity including mentorship as well as for the critical review of the data curation and the writing of the draft. I. Martínez-Visús is responsible for conducting the research, performing the synthesis of materials. M.J. Lázaro is responsible for management and coordination for the research activity planning and execution, as well as responsible for the acquisition of the financial support for the project leading to this publication, and for the critical review of the manuscript. All authors have supervised and critically revised the writing of the manuscript.

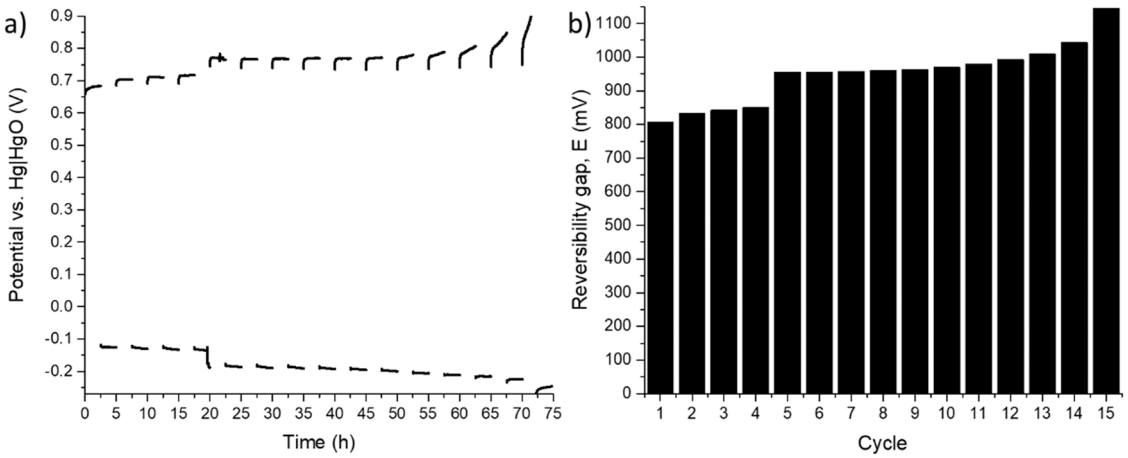

Fig. 9. a) Chronopotentiometric cycles and b) reversibility gap for each cycle for durability tests over catalyst 5Fe-MONW-120/CNF in GDE. Test carried out at ± 10 mA cm^{-2} and 2.5 h for each reaction in 6 M KOH.

Declaration of Competing Interest

The authors declare that they have no known competing financial interests or personal relationships that could have appeared to influence the work reported in this paper.

Data Availability

Data will be made available on request.

Acknowledgments

The authors wish to acknowledge the grant PID2020-115848RB-C21 funded by MCIN/AEI/10.13039/501100011033. Authors also acknowledge Gobierno de Aragón (DGA) for the financial support to Grupo de Conversión de Combustibles (T06_20R). N. Villanueva-Martínez also acknowledges DGA for his pre-doctoral contract.

Appendix A. Supporting information

Supplementary data associated with this article can be found in the online version at doi:10.1016/j.cattod.2023.114083.

References

[1] W.J. Kwak, D. Rosy, C. Sharon, H. Xia, L.R. Kim, P.G. Johnson, L.F. Bruce, Y. K. Nazar, A.A. Sun, M. Frimer, S.A. Noked, D. Freunberger, Aurbach, Lithium-oxygen batteries and related systems: potential, status, and future, ACS Appl. Mater. Interfaces 120 (14) (2020) 6626–6683, https://doi.org/10.1021/acs.chemrev.9b00609.

[2] Q. Liu, Z. Pan, E. Wang, L. An, G. Sun, Aqueous metal-air batteries: fundamentals and applications, Energy Storage Mater. 27 (2020) 478–505, https://doi.org/10.1016/j.ensm.2019.12.011.

[3] A. Kraytsberg, Y. Ein-Eli, The impact of nano-scaled materials on advanced metal-air battery systems, Nano Energy 2 (2013) 468–480, https://doi.org/10.1016/j.nanoen.2012.11.016.

[4] N.R. Levy, P. Tereshchuk, A. Natan, R. Haas, D. Schröder, J. Janek, P. Jakes, R. A. Eichel, Y. Ein-Eli, Hybridization of carbon nanotube tissue and MnO2 as a generic advanced air cathode in metal–air batteries, J. Power Sources 514 (2021), 230597, https://doi.org/10.1016/j.jpowsour.2021.230597.

[5] H. Weinrich, Y.E. Durmus, H. Tempel, H. Kungl, R.-A. Eichel, Silicon and iron as resource-efficient anode materials for ambient-temperature metal-air batteries, A Rev., Mater. Vol. 12 (2019) 2134, https://doi.org/10.3390/MA12132134.

[6] Y. Li, J. Lu, Metal-air batteries: will they be the future electrochemical energy storage device of choice? ACS Energy Lett. 2 (6) (2017) 1370–1377, https://doi.org/10.1021/acsenergylett.7b00119.

[7] H. Li, L. Ma, C. Han, Z. Wang, Z. Liu, Z. Tang, C. Zhi, Advanced rechargeable zinc-based batteries: recent progress and future perspectives, Nano Energy 62 (2019) 550–587, https://doi.org/10.1016/J.NANOEN.2019.05.059.

[8] X. Cai, L. Lai, J. Lin, Z. Shen, Recent advances in air electrodes for Zn-air batteries: electrocatalysis and structural design, Mater. Horiz. 4 (2017) 945–976, https://doi.org/10.1039/c7mh00358g.

[9] N.-T. Suen, S.-F. Hung, Q. Quan, N. Zhang, Y.-J. Xu, H.M. Chen, Electrocatalysis for the oxygen evolution reaction: recent development and future perspectives, Chem. Soc. Rev. 46 (2017) 337–365, https://doi.org/10.1039/C6CS00328A.

[10] M. Shao, Q. Chang, J.-P. Dodelet, R. Chenitz, Recent advances in electrocatalysts for oxygen reduction reaction, Chem. Rev. 116 (2016) 3594–3657, https://doi.org/10.1021/acs.chemrev.5b00462.

[11] C. Alegre, E. Modica, C. Lo Vecchio, S. Siracusano, A.S. Aricò, V. Baglio, Pd supported on Ti-suboxides as bifunctional catalyst for air electrodes of metal-air batteries, Int. J. Hydrog. Energy 41 (2016) 19579–19586, https://doi.org/10.1016/j.ijhydene.2016.03.095.

[12] R.D. McKerracher, H.A. Figueredo-Rodríguez, C. Ponce de León, C. Alegre, V. Baglio, A.S. Aricò, F.C. Walsh, A high-performance, bifunctional oxygen electrode catalysed with palladium and nickel-iron hexacyanoferrate, Electrochim. Acta 206 (2016) 127–133, https://doi.org/10.1016/j.electacta.2016.04.090.

[13] C. Alegre, S. Siracusano, E. Modica, A.S. Aricò, V. Baglio, Titanium–tantalum oxide as a support for Pd nanoparticles for the oxygen reduction reaction in alkaline electrolytes, Mater. Renew. Sustain. Energy 7 (2018) 8, https://doi.org/10.1007/s40243-018-0114-z.

[14] A.A. Gewirth, J.A. Varnell, A.M. Diascro, Nonprecious metal catalysts for oxygen reduction in heterogeneous aqueous systems, Chem. Rev. 118 (2018) 2313–2339, https://doi.org/10.1021/acs.chemrev.7b00335.

[15] R. Wang, Z. Chen, N. Hu, C. Xu, Z. Shen, J. Liu, Nanocarbon-based electrocatalysts for rechargeable aqueous Li/Zn-Air batteries, ChemElectroChem 5 (2018) 1745–1763, https://doi.org/10.1002/celc.201800141.

[16] Q. Wei, Y. Fu, G. Zhang, S. Sun, Rational design of carbon-based oxygen electrocatalysts for zinc–air batteries, Curr. Opin. Electrochem. 4 (2017) 45–59, https://doi.org/10.1016/J.COELEC.2017.09.006.

[17] X. Ge, A. Sumboja, D. Wuu, T. An, B. Li, F.W.T. Goh, T.S.A. Hor, Y. Zong, Z. Liu, Oxygen reduction in alkaline media: from mechanisms to recent advances of catalysts, ACS Catal. 5 (2015) 4643–4667, https://doi.org/10.1021/acscatal.5b00524.

[18] C. Alegre, E. Modica, M. Rodlert-Bacilieri, F.C. Mornaghini, A.S. Aricò, V. Baglio, Enhanced durability of a cost-effective perovskite-carbon catalyst for the oxygen evolution and reduction reactions in alkaline environment, Int. J. Hydrog. Energy 42, Issue 46, (2017), 28063-28069. doi:10.1016/j.ijhydene.2017.03.216.

[19] C. Alegre, C. Busacca, A. Di Blasi, O. Di Blasi, A.S.S. Aricò, V. Antonucci, E. Modica, V. Baglio, Electrospun carbon nanofibers loaded with spinel-type cobalt oxide as bifunctional catalysts for enhanced oxygen electrocatalysis, J. Energy Storage 23 (2019) 269–277, https://doi.org/10.1016/J.EST.2019.04.001.

[20] J.M. Luque-Centeno, M.V. Martínez-Huerta, D. Sebastián, G. Lemes, E. Pastor, M. J. Lázaro, Bifunctional N-doped graphene Ti and Co nanocomposites for the oxygen reduction and evolution reactions, Renew. Energy 125 (2018) 182–192, https://doi.org/10.1016/J.RENENE.2018.02.073.

[21] P. Stelmachowski, A.H.A. Monteverde Videla, T. Jakubek, A. Kotarba, S. Specchia, The Effect of Fe, Co, and Ni Structural Promotion of Cryptomelane (KMn8O16) on the Catalytic Activity in Oxygen Evolution Reaction, Electrocatalysis 9 (2018) 762–769, https://doi.org/10.1007/s12678-018-0488-9.

[22] A. Kostuch, J. Gryboś, P. Indyka, L. Osmieri, S. Specchia, Z. Sojka, K. Kruczała, Morphology and dispersion of nanostructured manganese-cobalt spinel on various carbon supports: The effect on the oxygen reduction reaction in alkaline media, Catal. Sci. Technol. 8 (2018) 642–655, https://doi.org/10.1039/c7cy02228j.

[23] H. Osgood, S.V. Devaguptapu, H. Xu, J. Cho, G. Wu, Transition metal (Fe, Co, Ni, and Mn) oxides for oxygen reduction and evolution bifunctional catalysts in alkaline media, Nano Today 11 (2016) 601–625, https://doi.org/10.1016/J.NANTOD.2016.09.001.

[24] A.B. Haruna, K.I. Ozoemena, Manganese-based bifunctional electrocatalysts for zinc-air batteries, Curr. Opin. Electrochem. 21 (2020) 219–224, https://doi.org/10.1016/J.COELEC.2020.02.021.

[25] L. Tian, X. Zhai, X. Wang, J. Li, Z. Li, Advances in manganese-based oxides for oxygen evolution reaction, J. Mater. Chem. A 8 (2020) 14400–14414, https://doi.org/10.1039/d0ta05116k.

[26] J. Deng, S. Fang, Y. Fang, Q. Hao, L. Wang, Y.H. Hu, Multiple roles of graphene in electrocatalysts for metal-air batteries, Catal. Today 409 (2023) 2–22, https://doi.org/10.1016/j.cattod.2022.01.003.

[27] M.F.P. Duarte, I.M. Rocha, J.L. Figueiredo, C. Freire, M.F.R. Pereira, CoMn-LDH@carbon nanotube composites: Bifunctional electrocatalysts for oxygen reactions, Catal. Today 301 (2018) 17–24, https://doi.org/10.1016/j.cattod.2017.03.046.

[28] M. Yin, H. Miao, R. Hu, Z. Sun, H. Li, Manganese dioxides for oxygen electrocatalysis in energy conversion and storage systems over full pH range, J. Power Sources 494 (2021), 229779, https://doi.org/10.1016/j.jpowsour.2021.229779.

[29] Y. Gu, G. Yan, Y. Lian, P. Qi, Q. Mu, C. Zhang, Z. Deng, Y. Peng, MnIII-enriched α-MnO2 nanowires as efficient bifunctional oxygen catalysts for rechargeable Zn-air batteries, Energy Storage Mater. 23 (2019) 252–260, https://doi.org/10.1016/j.ensm.2019.05.006.

[30] H. Singh, M. Marley-Hines, S. Chakravarty, M. Nath, Multi-walled carbon nanotube supported manganese selenide as a highly active bifunctional OER and ORR electrocatalyst, J. Mater. Chem. A 10 (2022) 6772–6784, https://doi.org/10.1039/d1ta09864k.

[31] J. Melder, S. Mebs, P.A. Heizmann, R. Lang, H. Dau, P. Kurz, Carbon fibre paper coated by a layered manganese oxide: a nano-structured electrocatalyst for water-oxidation with high activity over a very wide pH range, J. Mater. Chem. A 7 (2019) 25333–25346, https://doi.org/10.1039/C9TA08804K.

[32] H. Miao, B. Chen, S. Li, X. Wu, Q. Wang, C. Zhang, Z. Sun, H. Li, All-solid-state flexible zinc-air battery with polyacrylamide alkaline gel electrolyte, J. Power Sources 450 (2020), 227653, https://doi.org/10.1016/J.JPOWSOUR.2019.227653.

[33] T. Zhang, Z. Li, L. Wang, P. Sun, Z. Zhang, S. Wang, Spinel MnCo2O4 nanoparticles supported on three-dimensional graphene with enhanced mass transfer as an efficient electrocatalyst for the oxygen reduction reaction, ChemSusChem 11 (2018) 2730–2736, https://doi.org/10.1002/CSSC.201801070.

[34] C. Alegre, C. Busacca, A. Di Blasi, O. Di Blasi, A.S. Aricò, V. Antonucci, V. Baglio, Electrocatalysis of oxygen on bifunctional nickel-cobaltite spinel, ChemElectroChem 7 (2020) 124–130, https://doi.org/10.1002/celc.201901584.

[35] A. Mathur, A. Halder, One-step synthesis of bifunctional iron-doped manganese oxide nanorods for rechargeable zinc-air batteries, Catal. Sci. Technol. 9 (2019) 1245–1254, https://doi.org/10.1039/c8cy02498g.

[36] D. Sebastián, I. Suelves, R. Moliner, M.J. Lázaro, The effect of the functionalization of carbon nanofibers on their electronic conductivity, Carbon 48 (2010) 4421–4431, https://doi.org/10.1016/j.carbon.2010.07.059.

[37] Y. Ma, R. Wang, H. Wang, J. Key, S. Ji, Control of MnO2 nanocrystal shape from tremella to nanobelt for ehancement of the oxygen reduction reaction activity, J. Power Sources 280 (2015) 526–532, https://doi.org/10.1016/j.jpowsour.2015.01.139.

[38] W. Xiao, D. Wang, X.W. Lou, Shape-controlled synthesis of MnO2 nanostructures with enhanced electrocatalytic activity for oxygen reduction, J. Phys. Chem. C. 114 (2010) 1694–1700, https://doi.org/10.1021/jp909386d.

[39] M.C. Biesinger, B.P. Payne, A.P. Grosvenor, L.W.M. Lau, A.R. Gerson, R.S.C. Smart, Resolving surface chemical states in XPS analysis of first row transition metals, oxides and hydroxides: Cr, Mn, Fe, Co and Ni, Appl. Surf. Sci. 257 (2011) 2717–2730, https://doi.org/10.1016/j.apsusc.2010.10.051.

[40] D. Briggs, Handbook of X-ray Photoelectron Spectroscopy, in: C.D. Wanger, W. M. Riggs, L.E. Davis, J.F. Moulder, G. E.Muilenberg (Eds.), Physical Electronics Division, Perkin-Elmer Corp., Eden Prairie, Minnesota, USA, 1979, 190 pp., Surf. Interface Anal. 3 (1981) v–v. doi:10.1002/sia.740030412.

[41] V.P. Santos, M.F.R. Pereira, J.J.M. Órfão, J.L. Figueiredo, The role of lattice oxygen on the activity of manganese oxides towards the oxidation of volatile organic compounds, Appl. Catal. B Environ. 99 (2010) 353–363, https://doi.org/10.1016/j.apcatb.2010.07.007.

[42] H. Abdel-Samad, P.R. Watson, An XPS study of the adsorption of chromate on goethite (α-FeOOH), Appl. Surf. Sci. 108 (1997) 371–377, https://doi.org/10.1016/S0169-4332(96)00609-5.

[43] L. Li, X. Feng, Y. Nie, S. Chen, F. Shi, K. Xiong, W. Ding, X. Qi, J. Hu, Z. Wei, L. J. Wan, M. Xia, Insight into the Effect of Oxygen Vacancy Concentration on the Catalytic Performance of MnO2, ACS Catal. 5 (2015) 4825–4832, https://doi.org/10.1021/acscatal.5b00320.

[44] E. Hastuti, A. Subhan, P. Amonpattaratkit, M. Zainuri, S. Suasmoro, The effects of Fe-doping on MnO2: phase transitions, defect structures and its influence on electrical properties, RSC Adv. 11 (2021) 7808–7823, https://doi.org/10.1039/d0ra10376d.

[45] D. Mondal, B.K. Paul, S. Das, D. Bhattacharya, D. Ghoshal, P. Nandy, K. Das, S. Das, Synthesis and Property of Copper-Impregnated α-MnO2 Semiconductor Quantum Dots, Langmuir 34 (2018) 12702–12712, https://doi.org/10.1021/acs.langmuir.8b01745.

[46] D. Sebastián, I. Suelves, R. Moliner, M.J. Lázaro, The effect of the functionalization of carbon nanofibers on their electronic conductivity, Carbon 48 (15) (2010) 4421–4431, https://doi.org/10.1016/j.carbon.2010.07.059.

[47] M.S. Ahn, R. Ahmad, J.Y. Yoo, Y.B. Hahn, Synthesis of manganese oxide nanorods and its application for potassium ion sensing in water, J. Colloid Interface Sci. 516 (2018) 364–370, https://doi.org/10.1016/j.jcis.2018.01.081.

[48] J. Jia, P. Zhang, L. Chen, The effect of morphology of α-MnO2 on catalytic decomposition of gaseous ozone, Catal. Sci. Technol. 6 (2016) 5841–5847, https://doi.org/10.1039/c6cy00301j.

[49] J.C. Ruiz-Cornejo, D. Sebastián, M.J. Lázaro, Synthesis and applications of carbon nanofibers: a review, Rev. Chem. Eng. 36 (2020) 493–511, https://doi.org/10.1515/revce-2018-0021.

[50] D. Sebastián, A.G. Ruiz, I. Suelves, R. Moliner, M.J. Lázaro, On the importance of the structure in the electrical conductivity of fishbone carbon nanofibers, J. Mater. Sci. 48 (2013) 1423–1435, https://doi.org/10.1007/s10853-012-6893-1.

[51] C. Alegre, C. Busacca, A. Di Blasi, O. Di Blasi, A.S. Aricò, V. Antonucci, V. Baglio, Toward more efficient and stable bifunctional electrocatalysts for oxygen electrodes using FeCo2O4/carbon nanofiber prepared by electrospinning, Mater. Today, Energy 18 (2020), https://doi.org/10.1016/j.mtener.2020.100508.

[52] A. Holewinski, S. Linic, Elementary mechanisms in electrocatalysis: revisiting the ORR tafel slope, J. Electrochem. Soc. 159 (2012) H864–H870, https://doi.org/10.1149/2.022211jes.

[53] M. Shao, P. Liu, R.R. Adzic, Superoxide anion is the intermediate in the oxygen reduction reaction on platinum electrodes, J. Am. Chem. Soc. 128 (2006) 7408–7409.

[54] J.S. Spendelowa, A. Wieckowski, Electrocatalysis of oxygen reduction and small alcohol oxidation in alkaline media, Phys. Chem. Chem. Phys. 9 (2007) 2654–2675.

[55] T. Shinagawa, A.T. Garcia-Esparza, K. Takanabe, Insight on Tafel slopes from a microkinetic analysis of aqueous electrocatalysis for energy conversion, Sci. Rep. 5 (2015) 1–21, https://doi.org/10.1038/srep13801.

[56] F. Cheng, T. Zhang, Y. Zhang, J. Du, X. Han, J. Chen, Enhancing electrocatalytic oxygen reduction on MnO2 with vacancies, Angew. Chem. - Int. Ed. 52 (2013) 2474–2477, https://doi.org/10.1002/anie.201208582.

[57] F. Cheng, Y. Su, J. Liang, Z. Tao, J. Chen, MnO2-based nanostructures as catalysts for electrochemical oxygen reduction in alkaline media, Chem. Mater. 22 (2010) 898–905, https://doi.org/10.1021/cm901698s.

[58] T. Zhan, Y. Zhang, X. Liu, S.S. Lu, W. Hou, NiFe layered double hydroxide/reduced graphene oxide nanohybrid as an efficient bifunctional electrocatalyst for oxygen evolution and reduction reactions, J. Power Sources 333 (2016) 53–60, https://doi.org/10.1016/j.jpowsour.2016.09.152.

[59] M. Ma, A. Kumar, D. Wang, Y. Wang, Y. Jia, Y. Zhang, G. Zhang, Z. Yan, X. Sun, Boosting the bifunctional oxygen electrocatalytic performance of atomically dispersed Fe site via atomic Ni neighboring, Appl. Catal. B Environ. 274 (2020), 119091, https://doi.org/10.1016/j.apcatb.2020.119091.

[60] B. Guo, J. Guo, W. Yang, X. Tian, X. Wang, Z. Xiang, M. Wu, Highly dispersed iron/nickel dual-sites in hierarchical porous carbon materials as high-performance bifunctional oxygen electrocatalysts for Zn-air batteries, Renew. Energy 201 (2022) 117–124, https://doi.org/10.1016/j.renene.2022.11.036.

[61] C. Shenghai, S. Liping, K. Fanhao, H. Lihua, Z. Hui, Carbon-coated MnCo2O4 nanowire as bifunctional oxygen catalysts for rechargeable Zn-air batteries, J. Power Sources 430 (2019) 25–31, https://doi.org/10.1016/j.jpowsour.2019.05.029.

[62] S. Peng, X. Han, L. Li, S. Chou, D. Ji, H. Huang, Y. Du, J. Liu, S. Ramakrishna, Electronic and defective engineering of electrospun CaMnO3 nanotubes for enhanced oxygen electrocatalysis in rechargeable Zinc–air batteries, Adv. Energy Mater. 8 (2018), 1800612, https://doi.org/10.1002/aenm.201800612.

[63] J. Zhang, M. Zhang, Y. Zeng, J. Chen, L. Qiu, H. Zhou, C. Sun, Y. Yu, C. Zhu, Z. Zhu, Single Fe atom on hierarchically porous S, N-codoped nanocarbon derived from porphyra enable boosted oxygen catalysis for rechargeable Zn-air batteries, Small 15 (2019) 1900307, https://doi.org/10.1002/smll.201900307.

[64] B. Guo, J. Guo, W. Yang, X. Tian, X. Wang, Z. Xiang, M. Wu, Highly dispersed iron/nickel dual-sites in hierarchical porous carbon materials as high-performance bifunctional oxygen electrocatalysts for Zn-air batteries, Renew. Energy 201 (2022) 117–124, https://doi.org/10.1016/j.renene.2022.11.036.

[65] Y. Liu, K. Sun, X. Cui, B. Li, J. Jiang, Defect-rich, graphenelike carbon sheets derived from biomass as efficient electrocatalysts for rechargeable zinc-air batteries, ACS Sustain. Chem. Eng. 8 (2020) 2981–2989, https://doi.org/10.1021/acssuschemeng.9b07621.

[66] S. Zhou, J. Zang, H. Gao, X. Tian, P. Tian, S. Song, Y. Wang, Deflagration method synthesizing N, S co-doped oxygen-functionalized carbons as a bifunctional catalyst for oxygen reduction and oxygen evolution reaction, Carbon 181 (2021) 234–245, https://doi.org/10.1016/j.carbon.2021.05.034.

[67] C. Shao, F. Liao, W. Zhu, Y. Zhang, M. Ma, J. Yang, K. Yin, M. Shao, B. Jiang, Carbon dots bridge NiO and Mn2O3 as highly efficient bifunctional oxygen electrocatalysts for rechargeable zinc-air batteries, Appl. Surf. Sci. 596 (2022), 153642, https://doi.org/10.1016/j.apsusc.2022.153642.

[68] D.M. Morales, M.A. Kazakova, S. Dieckhöfer, A.G. Selyutin, G.V. Golubtsov, W. Schuhmann, J. Masa, Trimetallic Mn-Fe-Ni oxide nanoparticles supported on multi-walled carbon nanotubes as high-performance bifunctional ORR/OER electrocatalyst in alkaline media, Adv. Funct. Mater. 30 (2020) 1905992, https://doi.org/10.1002/adfm.201905992.

[69] D. Ji, J. Sun, L. Tian, A. Chinnappan, T. Zhang, W.A.D.M. Jayathilaka, R. Gosh, C. Baskar, Q. Zhang, S. Ramakrishna, Engineering of the heterointerface of porous carbon nanofiber–supported nickel and manganese oxide nanoparticle for highly efficient bifunctional oxygen catalysis, Adv. Funct. Mater. 30 (2020) 1910568, https://doi.org/10.1002/adfm.201910568.

[70] A. Wahab, N. Iqbal, T. Noor, S. Ashraf, M.A. Raza, A. Ahmad, U.A. Khan, Thermally reduced mesoporous manganese MOF @reduced graphene oxide nanocomposite as bifunctional electrocatalyst for oxygen reduction and evolution, RSC Adv. 10 (2020) 27728–27742, https://doi.org/10.1039/d0ra04193a.

[71] X. Xiao, W. Zhang, H. Zhao, L. Li, P. Deng, Y. Wu, S. Luo, B. Chen, Ultrathin amorphous MnO2 modified prawn shells-derived porous carbon towards robust oxygen electrocatalyst for rechargeable Zn-air battery, Ceram. Int. 48 (5) (2022) 6506–6511, https://doi.org/10.1016/j.ceramint.2021.11.195.